Scalable Assembly of High-Quality Graphene Films via Electrostatic-Repulsion Aligning

Wei Qian, Huaqiang Fu, Yi Sun, Zhe Wang, Han Wu, Zongkui Kou, Bao-Wen Li,* Daping He,* and Ce-Wen Nan

Assembling pristine graphene into freestanding films featuring high electrical conductivity, superior flexibility, and robust mechanical strength aims at meeting the all-around high criteria of new-generation electronics. However, voids and defects produced in the macroscopic assembly process of graphene nanosheets severely degrade the performance of graphene films, and mechanical brittleness often limits their applications in wide scenarios. To address such challenges, an electrostatic-repulsion aligning strategy is demonstrated to produce highly conductive, ultraflexible, and multifunctional graphene films. Typically, the high electronegativity of titania nanosheets (TiNS) induces the aligning of negatively charged graphene nanosheets via electrostatic repulsion in the film assembly. The resultant graphene films show fine microstructure, enhanced mechanical properties, and improved electrical conductivity up to 1.285×10^5 S m^{-1}. Moreover, the graphene films can withstand 5000 repeated folding without structural damage and electrical resistance fluctuation. These comprehensive improved properties, combined with the facile synthesis method and scalable production, make these graphene films a promising platform for electromagnetic interference (EMI) shielding and thermal-management applications in smart and wearable electronics.

1. Introduction

The macroscopic assembly of graphene-based nanomaterials into freestanding films that possess excellent electrical conductivity, flexibility, and mechanical properties has attracted tremendous interest for various applications, such as electromagnetic interference (EMI) shielding,[1] energy storage,[2] sensors,[3] and wearable electronics devices.[4] Currently, graphene

oxide is used as the precursor for synthesis of graphene films,[5] since the good dispersion and processability of graphene oxide benefit for the fabrication of layered films. However, its electrical insulating and defect-rich features largely limit the realization of high-performance films. Major research interest of graphene preparation, therefore, lies in the reduction of graphene oxide by chemical or thermal treatment.[5d,6] Nevertheless, these treatment methods not only fail to remove the oxygen-containing functional groups to a large amount but also suffer from inevitable environmental pollution and prohibitive cost. In addition, various gas molecules such as water vapor, carbon monoxide, and carbon dioxide are generated during the reduction process,[5c,7] which usually leave a large amount of microsized voids in the films, decreasing their innate electrical and mechanical properties. Based on the above problems, it is necessary to find out an effective way to prepare high-performance graphene films with different raw materials.

In comparison with graphene oxide, pristine graphene (PG) with low fraction of defects exhibits satisfying electrical conductivity, low density, and outstanding mechanical properties.[8] It has been demonstrated that planar carbon bonding of graphene exhibits extremely high electrical conductivity[9] and tensile strength.[10] However, these remarkable innate properties of

---

W. Qian, Z. Wang, D. He
Hubei Engineering Research Center of Radio Frequency
Microwave Technology and Application
Wuhan University of Technology
Wuhan 430070, P. R. China
E-mail: hedaping@whut.edu.cn
H. Fu, D. He
State Key Laboratory of Silicate Materials for Architectures
Wuhan University of Technology
Wuhan 430070, P. R. China

Y. Sun, H. Wu, B.-W. Li
State Key Laboratory of Advanced Technology for Materials
Synthesis and Processing
Center of Smart Materials and Devices
Wuhan University of Technology
Wuhan 430070, P. R. China
E-mail: bwli@whut.edu.cn
Z. Kou
State Key Laboratory of Advanced Technology for Materials
Synthesis and Processing
Wuhan University of Technology
Wuhan 430070, P. R. China
C.-W. Nan
State Key Lab of New Ceramics and Fine Processing
School of Materials Science and Engineering
Tsinghua University
Beijing 100084, P. R. China

**ADVANCED
SCIENCE NEWS**

www.advancedsciencenews.com

**ADVANCED
MATERIALS**

www.advmat.de

graphene are limited at the nanoscale. When PG nanosheets are assembled into macrostructure such as graphene films, their electrical and mechanical properties are several orders of magnitude lower than those of individual PG nanosheet. This discrepancy is mainly due to the agglomeration of PG nanosheets caused by van der Waals attraction and π–π stacking,[11] which leads to structural defects in the assembly process, including lamellar dislocation, numerous wrinkles, and voids, which ultimately lead to the brittleness of graphene films and limit the improvements of their electrical and mechanical properties. Therefore, removing the structural defects is essential to improving the overall properties of graphene films. Various approaches have been reported previously to obtain stable graphene dispersions, including introduction of covalent and noncovalent functionalization of graphene nanosheets,[12] selecting of organic solvents with a low enthalpy,[13] and generating electrostatic repulsion between graphene nanosheets by adding surfactant[14] or protonation.[15] However, these approaches also have their drawbacks. For example, organic solvents are potentially hazardous to users and the environment. Surface functionalization and surfactants reduce mechanical and electrical properties of products. Hence, high concentration and stable aqueous graphene dispersions are highly desirable without complicated chemical reagents and processes.

In this work, we fabricate highly aligned and densely packed graphene hybrid films by adding only a small amount of unilamellar titania nanosheets (TiNS). High electronegativity of TiNS improves the electrostatic interaction between PG nanosheets and enhances the fluidity of suspensions, which is beneficial to suppress the re-stacking and improve the ordered arrangement of PG nanosheets, thereby promoting ordered self-assembly of PG nanosheets. The obtained graphene hybrid films exhibit significantly improved mechanical flexibility and electrical properties due to the decrease of the internal structure defects. These comprehensive improved properties, combined with the facile synthesis method and scalable production, make the assembled graphene films a promising platform for EMI shielding and thermal management applications in smart and wearable electronics.

2. Results and Discussion

The suspension of few-layer PG nanosheets of about 2.8 nm in thickness and several micrometers in lateral size was mechanically exfoliated from expandable graphite (Figure S1, Supporting Information). Unilamellar TiNS were synthesized as before,[16] and detailed procedures are described in the Experimental Section (Figure S2, Supporting Information). As shown in the transmission electron microscopy (TEM) image, the lateral sizes of unilamellar TiNS were in the range of 0.1–1 µm (Figure S3a,b, Supporting Information). The atomic force microscopy (AFM) image shows that the thickness of the obtained TiNS was about 1.5 nm (Figure S3c,d, Supporting Information).

The freestanding graphene hybrid films were fabricated by tape casting the dispersion of few-layer PG nanosheets with a low loading of TiNS, as illustrated in **Figure 1**a, which is a simple and promising manufacturing technology for mass production at low cost. We obtained various PG–TiNS hybrid films by changing the weight ratio x of TiNS, denoted as PG–TiNSx.

The morphological features of hybrid films are investigated in Figure 1. Compared with the light black of PG dispersion, the color of hybrid PG dispersion exhibits dark black (Figure S4, Supporting Information). This change in appearance also implies a difference in inner structure and compositional characteristics. In the subsequent drying process, there were many cracks appearing on the surface of the PG film, while the PG–TiNS5 film can keep its structural integrity without any cracks. Cross-sectional scanning electron microscopy (SEM) observation clearly demonstrates that randomly undulating and loosely layers gradually transform into parallel and dense lamellar structures with the increase of TiNS content from 0% to 5% (Figure 1b,c; Figure S5, Supporting Information). It is worth noting that the nanosheets in the PG–TiNS5 film adhere to each other to form a continuous parallel lamellar structure, which is obviously distinct from the individual separation of the nanosheets in the PG film. Accordingly, the thickness of the PG–TiNS5 film (48 µm) is nearly half of the PG film (95 µm), indicating that the voids in the PG hybrid films are effectively eliminated. Top-view SEM images clearly show that with the increase of the TiNS content, the microcracks and voids on the surface of the hybrid film gradually decrease until they are almost invisible (Figure 1d; Figure S6, Supporting Information). Meanwhile, the surface roughness of samples was examined using both a super large depth of the field 3D microscopic system and AFM (Figure $1e_1$–f_2; Figure S7, Supporting Information). It can be clearly seen that the PG–TiNS5 film is flatter than the PG film (Figure $1e_1,e_2$). The surface of the PG film is hill like with a root-mean-square (RMS) roughness value of 466 nm, while the PG–TiNS5 film exhibits a relatively smooth surface with RMS roughness reduced to 160 nm. These results consistently demonstrate that the PG–TiNS5 film has a more compact and flatter structure than the PG film. Therefore, the apparent density of the PG–TiNS5 film increased from 0.49 to 1.43 g cm^{-3} due to the decrease of thickness in the vertical and decrease of cracks in the parallel. Moreover, cross-sectional SEM images and the corresponding elemental mapping of C, O, and Ti confirm that TiNS is uniformly dispersed throughout the hybrid film volume without obvious localized agglomeration (Figure 1g).

The orientation degree of the nanosheets was further investigated quantitatively by small-angle X-ray scattering (SAXS) and wide-angle X-ray scattering (WAXS) tests. The PG–TiNS5 film exhibits a higher equatorial streak scattering and a narrower intensity distribution in the azimuthal angle direction[17] (**Figure 2**a). The calculated Herman's orientation factors (f) from SAXS and WAXS scattering are as high as 83.1 and 80.3, respectively, higher than those for the PG film (81.1 and 79.1) (Figure S8, Supporting Information). As illustrated in Figure 2b, we demonstrate that the thickness, porosity, and density of hybrid films can be precisely regulated by means of adjusting content of TiNS, and the results show that the thickness and porosity diminish linearly and the density increases linearly with the increasing TiNS content. Taken together, these results consistently confirm that TiNS promotes such neat and compact stacking of PG nanosheets, resulting
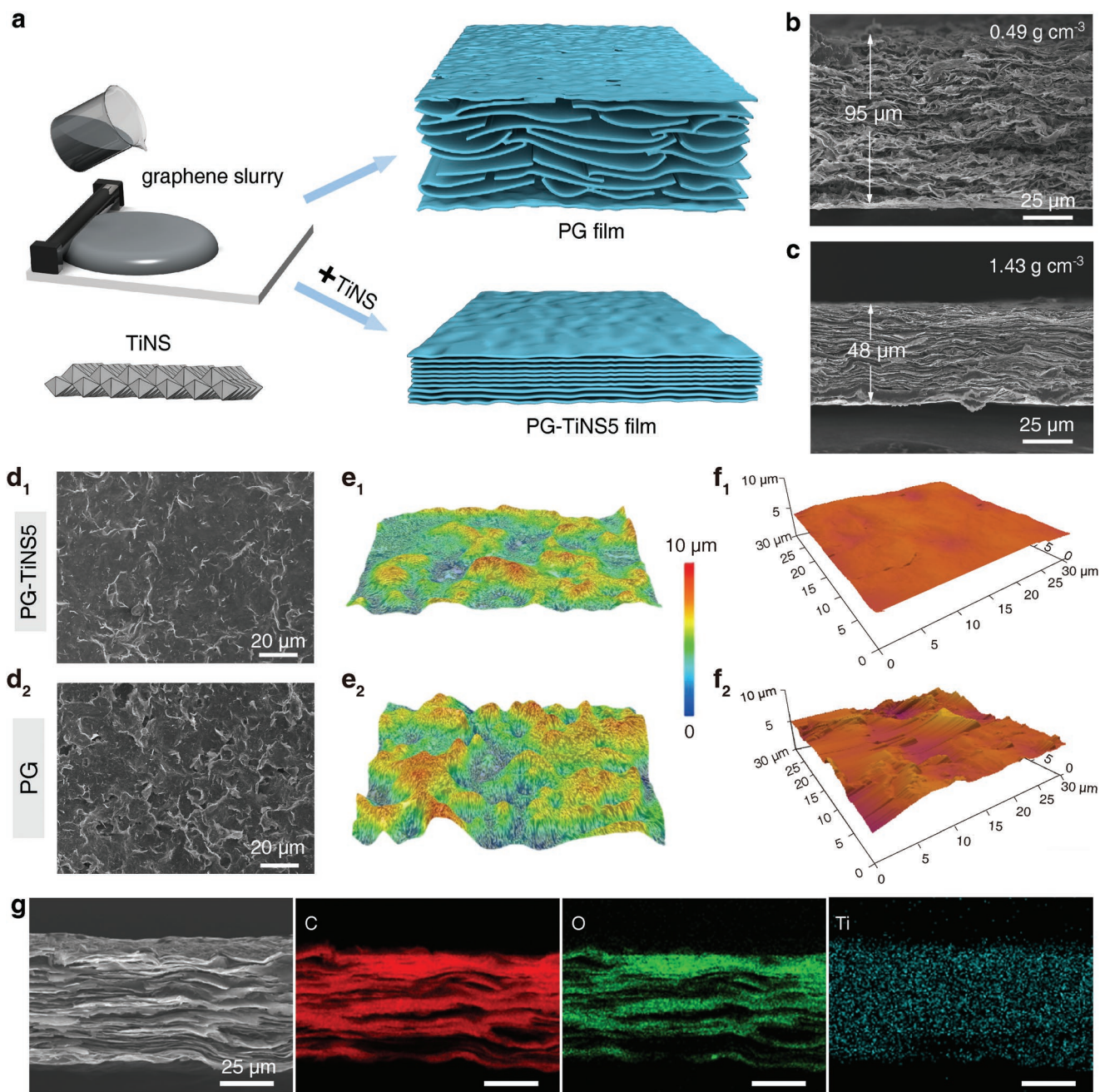
**ADVANCED
SCIENCE NEWS**

www.advancedsciencenews.com

**ADVANCED
MATERIALS**

www.advmat.de

Figure 1. Fabrication and characterization of PG and PG–TiNS5 films. a) Schematic of the fabrication procedure and the morphological comparison between PG and PG–TiNS hybrid films. b,c) Cross-sectional SEM images of b) PG and c) PG–TiNS5 films. d_1–f_2) Top-view SEM, optical, and AFM images of PG–TiNS5 (d_1–f_1) and PG (d_2–f_2) films, respectively. g) Cross-sectional SEM image of PG hybrid film and corresponding elemental maps of C, O, and Ti.

in greatly improved layer alignment. Ultimately, highly aligned and dense hybrid films were obtained.

The presence of agglomeration and wrinkles of PG nanosheets would generate irregularly aligned and loosely stacked lamellar structures,[5b] which severely degrades the electrical conductivity and mechanical properties of graphene films. In sharp contrast to the disordered phase of PG suspension, after adding a small amount of TiNS, the PG suspension evolves into long-range ordered lamellar liquid crystal phases

with characteristic bright and dark stripes in its polarized microscope (POM) image (Figure 2c,d; Figure S9, Supporting Information). Meanwhile, as shown in Figure 2e, considerable wrinkles and edge folding appear on the surface of PG. In contrast, we observe a significant wrinkle-flat transition in PG nanosheets after adding a small fraction of TiNS (Figure 2f). By such a design, additionally, as depicted in Figure 2g, the zeta potential values of PG, TiNS, and PG–TiNS5 were –11.2, –40.8, and –26.9 mV, respectively, which indicates that TiNS can
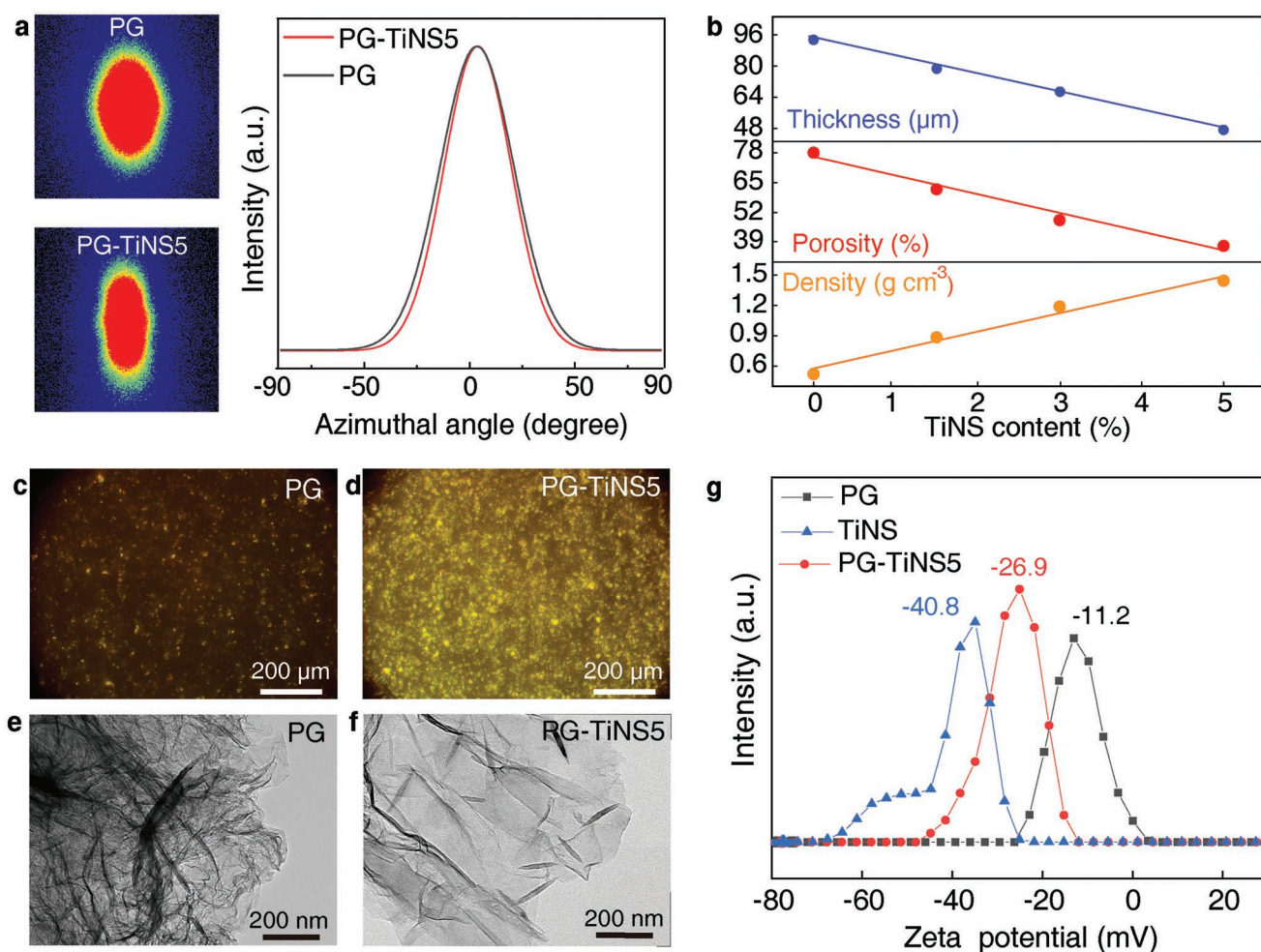
Figure 2. Morphological and structural analyses of PG and PG–TiNS5 films. a) 2D SAXS patterns and corresponding azimuthal angle plots of PG and PG–TiNS5 films. b) Linear relationship of density, porosity, and thickness with TiNS content. c,d) POM images of PG (c) and PG–TiNS5 (d). e,f) TEM images of crumpled PG (e) and flat PG–TiNS5 (f). g) Zeta potential values of PG, TiNS, and PG–TiNS5 solutions.

improve the electrostatic repulsion between PG nanosheets and enhance the fluidity of PG suspensions. Driven by external stirring and entropy effects,[18] the PG nanosheets become easier to assemble parallel to each other, thereby forming an ordered lamellar structure.

The microstructure and compositional characteristics of graphene films were demonstrated by X-ray photoelectron spectroscopy (XPS), energy-dispersive X-ray spectroscopy (EDS), X-ray diffraction (XRD), and Raman spectroscopy. The XPS spectra show that the C/O ratio in PG–TiNS5 film was 16.8, while 30.7 in the PG film (Figure S10, Supporting Information). The increase in oxygen element and the characteristic signal of Ti element appearing jointly confirmed the presence of TiNS. Sharp and intense diffraction peaks were both observed in PG and PG–TiNS5 films, with a nearly identical interlayer spacing of $d_{002} = 0.34$ nm, suggesting the formation of lamellar structure in the resulting films (Figure S11a, Supporting Information). Raman spectroscopy was employed to further characterize the defects including sp^3 hybridization and kinks[19] (Figure S11b, Supporting Information). The ratio of peak intensity for D peak and G peak (I_D/I_G) of PG film was about 0.11, two times higher

than that of the PG–TiNS5 hybrid film of 0.06. This result further indicates that there are a fewer structural defects in the PG–TiNS5 film.

The densification and orientation enhancement of the graphene films significantly improve the mechanical properties and flexibility. The tensile strength and elongation at break of the PG–TiNS5 film are as high as 8.18 ± 0.88 MPa and 2.24 ± 0.38%, ≈3.8 and ≈2.2 times higher that than those of PG film (2.13 ± 0.16 MPa, 1.03 ± 0.16%), respectively (**Figure 3**a,b). As shown in Figure 3c, closer inspections reveal a jagged edge in the fracture of PG–TiNS5 film, which is supposed to arrest the crack propagation and dissipate more energy. In contrast, the PG film exhibits a straight crack similar to an "H" shape (Figure 3d), implying a brittle fracture. It can be observed from the folded PG–TiNS5 and PG films, when being folded in half, PG–TiNS5 film remains tightly stacked with an intact structure (Figure 3e), while PG film is broken in the bended region (Figure 3f). Furthermore, the cross-sectional SEM image of the PG–TiNS film clearly presents a more ordered structure; thus, the degree of overlapping and interaction force between 2D nanosheets are significantly stronger. Obvious voids and a
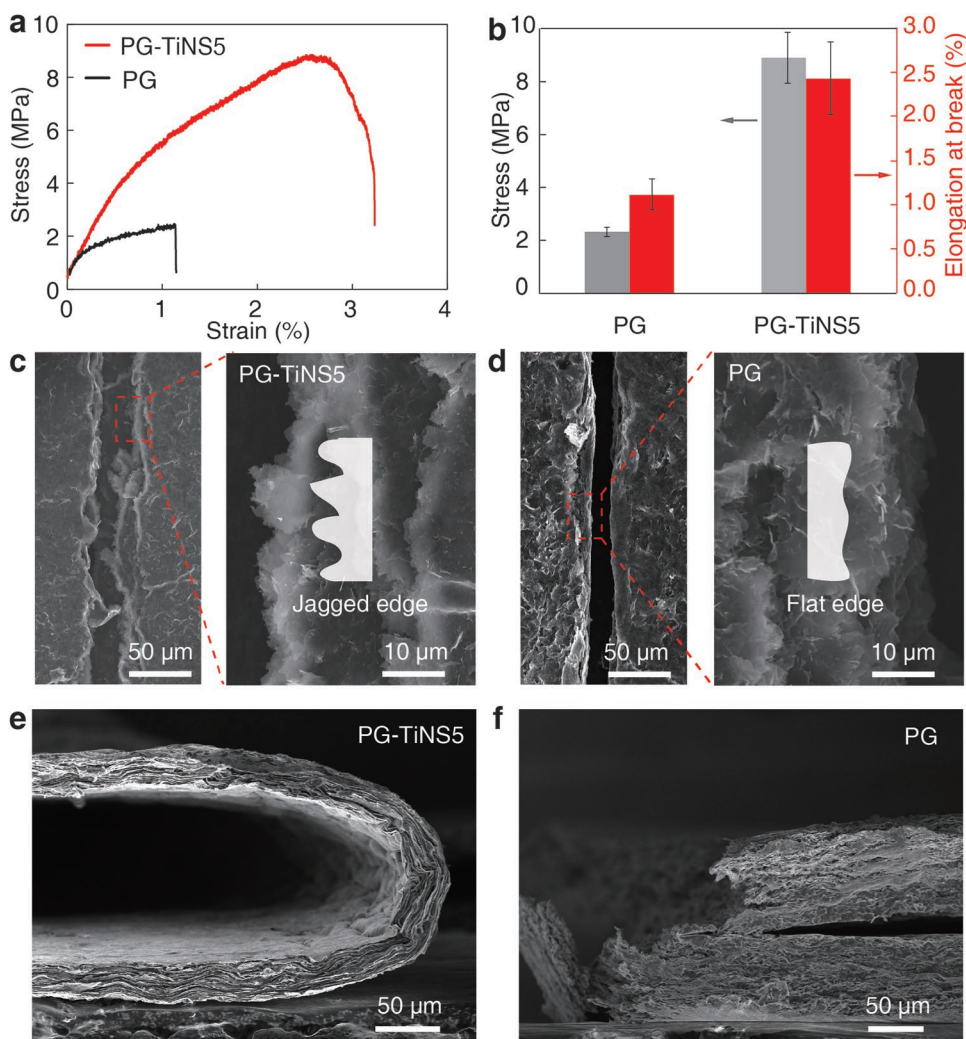
**ADVANCED
SCIENCE NEWS**
www.advancedsciencenews.com

**ADVANCED
MATERIALS**
www.advmat.de

Figure 3. Mechanical properties of PG and PG–TiNS5 films. a) Representative stress–strain curves of PG and PG–TiNS5 films. b) Calculated tensile stress and elongation at break. c,d) Fracture morphology of top-view SEM of PG–TiNS5 (c) and PG (d) films. e,f) Cross-sectional SEM images of PG–TiNS5 (e) and PG (f) films folded at 180°.

cluttered structure appear in PG film, while negligible voids are observed on the surface of PG–TiNS5 film. Our observations suggest that the hybrid film presents better mechanical strength, excellent flexibility, and mechanical stability, which should be ascribed to highly aligned and compact structures induced by TiNS.

Such a compact stacking structure in the highly aligned hybrid film not only contributes to the increase of mechanical strength but also significantly improves the electrical conductivity. The prepared the PG–TiNS5 film shows high electrical conductivity reaching up to 1.285×10^5 S m^{-1}, nearly seven times larger than that of the PG film (**Figure 4**a; Figure S12a,b, Supporting Information). As illustrated in Figure 4b and Table S1 (Supporting Information), the electrical conductivity of the PG–TiNS5 film is higher than that of almost all previously reported PG-based films. Such a high electrical conductivity is mainly attributed to the compact structure and high orientation of the hybrid film, which is beneficial for the charge transfer. In addition, after 5000 cycles of compressing and stretching, the electrical resistance of the PG–TiNS5 film is nearly unchanged (Figure 4c,d), indicating its remarkable stability and flexibility. The folding angle used for the flexibility test is 180°. Meanwhile, the structural integrity of the PG–TiNS film was maintained in water and phosphate-buffered solution (PBS) for 1 week (Figure S13, Supporting Information), demonstrating excellent stability.

The electrical conductivity is the dominant factor in determining the EMI shielding effectiveness (SE) of a material.[20] Compared with PG film, the excellent electrical conductivity endows PG–TiNS5 film with a thickness of 54 µm, and a high EMI SE of 74 dB at 8.2–12.4 GHz (**Figure 5**a; Figure S12c, Supporting Information), which indicates that almost 100% of the incident radiation can be blocked, therefore fully meeting the requirements of EMI shielding for commercial applications.[21] The EMI SE results of PG–TiNS5 film are obviously higher than PG film with the same thickness (57 dB). Moreover, the measured EMI SE value of the 54 µm-thick PG–TiNS5 film is highly consistent with the theoretical value calculated using Simon's formula (Figure S12d, Supporting Information).[22] The Simon's
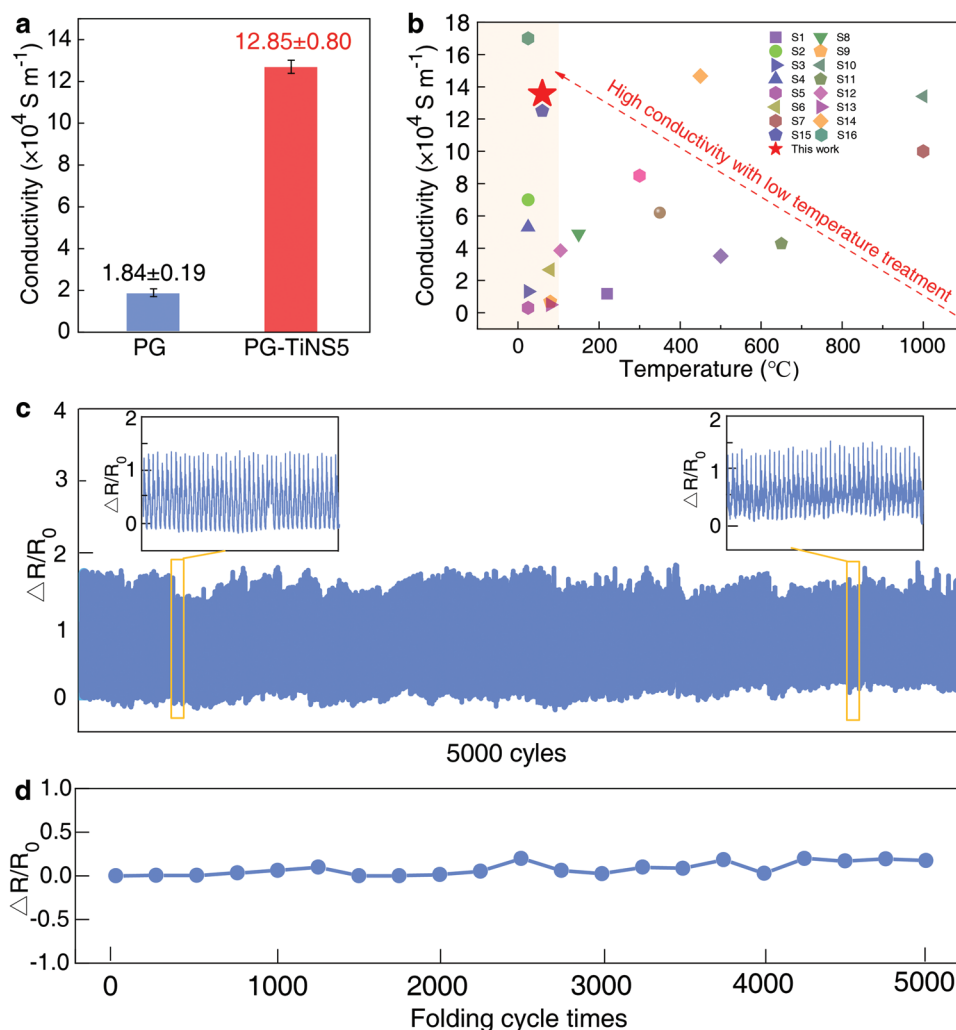
ADVANCED
SCIENCE NEWS
www.advancedsciencenews.com

ADVANCED
MATERIALS
www.advmat.de

Figure 4. Electrical performance of PG and PG–TiNS5 films. a) Electrical conductivity of PG and PG–TiNS5 films. b) Comparison of the electrical conductivity of PG–TiNS5 film with other PG-based films under different treatment temperatures. The numbers in (b) are the reference numbers listed in Table S1(Supporting Information). c) Variation in resistance of the PG–TiNS5 film to show its long-term durability. d) Changes in resistance of the PG–TiNS5 film during 5000 folding times.

formula can be expressed as SE = $50 + 10\log(\sigma/f) + 1.7t(\sigma f)^{1/2}$, where σ is the electrical conductivity (S cm^{-1}), f is the frequency (MHz), and t is the thickness of the film (cm). To further analyze the EMI shielding mechanism, the relationship of power coefficients of reflection (R), absorption (A), and transmission (T) of PG–TiNS5 film was investigated (Figure S12e, Supporting Information). The value of R was significantly higher than that of A, which indicates that reflection is the dominant EMI shielding mechanism, rather than absorption. This is mainly because of the relatively large electrical conductivity of the films, which leads to impedance mismatch, and therefore, only a small part of EM can penetrate the film. As a result, over 99% of the EM is reflected at the surface of films. The overall EMI shielding effectiveness (SE_T), microwave reflection (SE_R), and microwave absorption (SE_A) are collected at 8.2 GHz (Figure S12f, Supporting Information). The value of SE_A is greater than SE_R, which means that only a very small amount of the EM penetration of the material surface is attenuated by multiple internal reflection and Ohmic loss.[23] Moreover,

the specific reliable parameter (SSE/t), defined as the EMI SE divided by density and thickness (t), is introduced to evaluate the EMI SE performance of PG–TiNS5 film. The SSE/t value of PG–TiNS5 film is 13 482 dB cm^2 g^{-1}, superior to most solid EMI shielding nanocomposites reported previously (Figure 5b; Table S2, Supporting Information).

The infrared (IR) thermal images of PG–TiNS5 film show that when the applied voltage is 1–3.5 V, the temperature increases uniformly (Figure S14, Supporting Information). Figure 5c shows the measured data and linear fitting between the current and the applied voltage. The current linearly increases with the applied voltage, indicating excellent stability at low resistance. In addition, the saturation temperature of the graphene films presents the nearly linear relationship with the square of the applied voltage (Figure S15a, Supporting Information), which is in accordance with Joule laws in theory. The cyclic heating tests of PG–TiNS5 film are performed by repeatedly applying a DC voltage of 3 V. Steady-state temperature remained stable after more than 20 cycles of the on–off heating
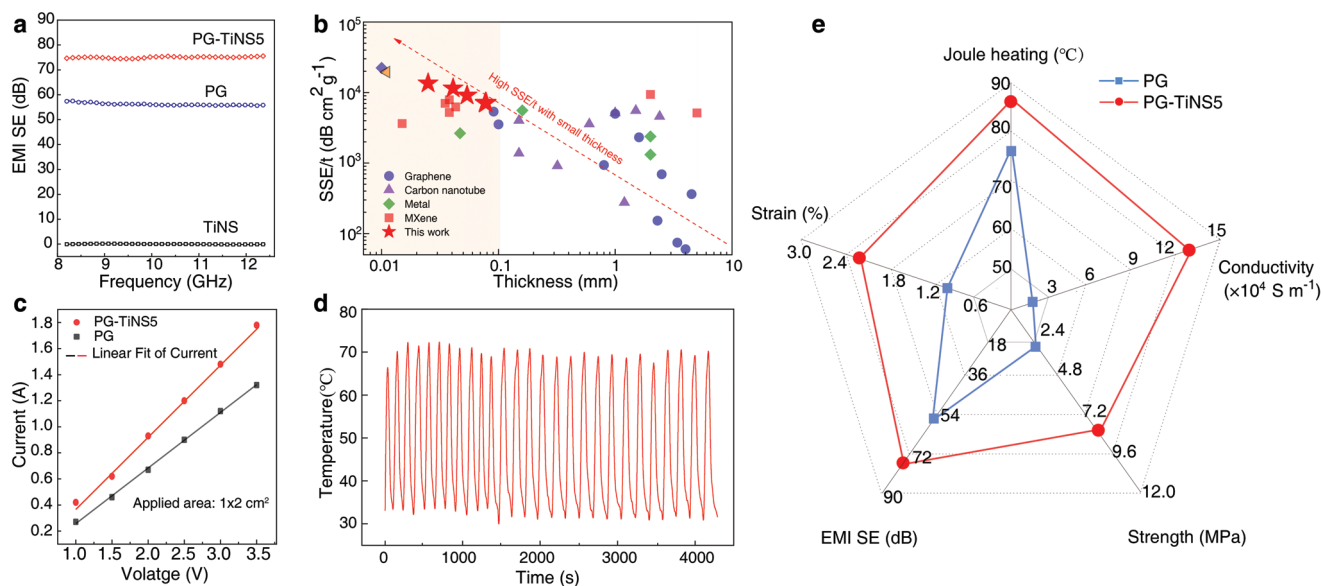
**ADVANCED
SCIENCE NEWS**

www.advancedsciencenews.com

**ADVANCED
MATERIALS**

www.advmat.de

Figure 5. EMI shielding and Joule heating performance of PG–TiNS hybrid films. a) EMI SE of the TiNS, PG, and PG–TiNS5 films plotted as a function of frequency, with the same thickness of 54 μm. b) Comparison of SSE/t values of PG–TiNS5 film with other solid EMI shielding nanocomposites. Detailed SSE/t date are listed in Table S2 (Supporting Information). c) I–V curves PG and PG–TiNS5 films. d) Cyclic stability test of PG–TiNS5 film by repeatedly applying a DC voltage of 3 V. e) A radar plot showing overall physical characterizations of PG and PG–TiNS5 films, including Joule heating, electrical conductivity, strength, strain, and EMI SE.

tests (Figure 5d; Figure S15b, Supporting Information). The surface temperatures of PG and PG–TiNS5 films increase from room temperature to 80.8 and 91.9 °C at the applied voltage range of 1.0–3.5 V (Figure S15c,d, Supporting Information), respectively, and the saturation temperature drops immediately after turning off the applied voltage. It can be seen that PG–TiNS5 film presents an excellent stable temperature at about 85 °C within the long duration of 2000 s, indicating the excellent long-term heating stability and reliability for the wearable heater (Figure S16, Supporting Information). A radar plot shows a direct visual comparison of the overall performances of PG–TiNS5 and PG films (Figure 5e). The PG–TiNS5 film exhibits superior performances in the aspects of electrical conductivity, tensile strength, breaking elongation, EMI SE, and Joule heating, demonstrating enormous potential for application in flexible and wearable electronic devices.

3. Conclusions

A well-confined graphene hybrid film has been realized by adding a small amount of TiNS to suppress the re-stacking of PG nanosheets and improve the ordered arrangement of PG nanosheets. The material preparation strategy reported here can well optimize the orientation and porosity of graphene films, and is easily scalable. As a result, significant improvement in the overall properties has been observed in the resultant films, including ultrahigh electrical conductivity, outstanding flexibility, robust mechanical performance, and excellent EMI SE. Such excellent comprehensive performances enable the PG–TiNS films enormous potential for many applications such as wearable electronics and next-generation portable devices.

4. Experimental Section

Materials: PG nanosheets were purchased from Harbin wanxin graphite valley Co. Ltd., mixed with polyvinyl pyrrolidone K60 (PVP60) and ultrapure water with a weight ratio of 1:0.2:30. TiNS was synthesized according to the previously reported method.[11] Typically, a layered compound of $K_{0.8}Ti_{1.73}Li_{0.27}O_4$ was synthesized by calcining the mixed chemicals of K_2CO_3, TiO_2, and Li_2CO_3 at 900 °C for 20 h. The layered titanate was then converted into $H_{1.07}Ti_{1.73}O_4$ in HCl solution. Colloidal suspension of unilamellar TiNS was obtained by delaminating $H_{1.07}Ti_{1.73}O_4$ crystals in an aqueous solution of tetramethylammonium hydroxide ((CH_3)$_4$NOH, TBAOH) with a solid-to-solution ratio of 4 mg mL^{-1}.

Fabrication of PG–TiNS films: The PG–TiNS hybrid films were produced by a blade casting method. Typically, PG nanosheets and TiNS were mixed into PG–TiNS solution. Five samples were prepared with different mass fractions of the TiNS such as 0, 1.5, 3.0, 5.0, and 7.0 wt%, respectively. The PG–TiNS dispersions were first stirred at 1000 rpm min^{-1} for 8 h to obtain their homogeneous dispersions. The dispersions were then bar-coated onto the poly(ethylene terephthalate) (PET) substrate with controllable thickness by changing the concentration and height of the dispersion followed by heating at 60 °C for 24 h to form the PG–TiNS hybrid film. Finally, the freestanding PG–TiNS hybrid films were obtained by peeling of the film from the PET substrate.

Supporting Information

Supporting Information is available from the Wiley Online Library or from the author.

Acknowledgements

Conflict of Interest

The authors declare no conflict of interest.

Data Availability Statement

The data that support the findings of this study are available from the corresponding author upon reasonable request.

Keywords

alignment control, electrical conductivity, electrostatic repulsion, pristine graphene, titania nanosheets

[1] a) S. Wan, Y. Chen, Y. Wang, G. Li, G. Wang, L. Liu, J. Zhang, Y. Liu, Z. Xu, A. P. Tomsia, L. Jiang, Q. Cheng, *Matter* **2019**, *1*, 389; b) T. Zhou, H. Ni, Y. Wang, C. Wu, H. Zhang, J. Zhang, A. P. Tomsia, L. Jiang, Q. Cheng, *Proc. Natl. Acad. Sci. USA* **2020**, *117*, 8727.

[2] Q. Wu, J. Yang, Y. Zhao, R. Song, Z. Wang, Z. Huang, M. Shi, Y. Ye, D. He, S. Mu, *J. Power Sources* **2020**, *455*, 227991.

[3] a) Z. Wang, P. Li, R. Song, W. Qian, H. Zhou, Q. Wang, Y. Wang, X. Zeng, L. Ren, S. Yan, S. Mu, D. He, *Sci. Bull.* **2020**, *65*, 1363; b) Y. Yang, Z. Cao, P. He, L. Shi, G. Ding, R. Wang, J. Sun, *Nano Energy* **2019**, *66*, 104134.

[4] a) K. Pan, Y. Fan, T. Leng, J. Li, Z. Xin, J. Zhang, L. Hao, J. Gallop, K. S. Novoselov, Z. Hu, *Nat. Commun.* **2018**, *9*, 5197; b) D. Tang, Q. Wang, Z. Wang, Q. Liu, B. Zhang, D. He, Z. Wu, S. Mu, *Sci. Bull.* **2018**, *63*, 574.

[5] a) J. Lin, P. Li, Y. Liu, Z. Wang, Y. Wang, X. Ming, C. Gao, Z. Xu, *ACS Nano* **2021**, *15*, 4824; b) P. Li, M. Yang, Y. Liu, H. Qin, J. Liu, Z. Xu, Y. Liu, F. Meng, J. Lin, F. Wang, C. Gao, *Nat. Commun.* **2020**, *11*, 2645; c) A. Akbari, B. V. Cunning, S. R. Joshi, C. Wang, D. C. Camacho-Mojica, S. Chatterjee, V. Modepalli, C. Cahoon, C. W. Bielawski, P. Bakharev, G. H. Kim, R. S. Ruoff, *Matter* **2020**, *2*, 1198; d) X. Chen, X. Deng, N. Y. Kim, Y. Wang, Y. Huang, L. Peng, M. Huang, X. Zhang, X. Chen, D. Luo, B. Wang, X. Wu, Y. Ma, Z. Lee, R. S. Ruoff, *Carbon* **2018**, *132*, 294.

[6] a) S. Pei, J. Zhao, J. Du, W. Ren, H. M. Cheng, *Carbon* **2010**, *48*, 4466; b) Y. Wen, M. Wu, M. Zhang, C. Li, G. Shi, *Adv. Mater.* **2017**, *29*, 1702831; c) B. Shen, W. Zhai, W. Zheng, *Adv. Funct. Mater.* **2014**, *24*, 4542.

[7] a) H. Huang, X. Ming, Y. Wang, F. Guo, Y. Liu, Z. Xu, L. Peng, C. Gao, *Carbon* **2021**, *180*, 197; b) E. Zhou, J. Xi, Y. Guo, Y. Liu, Z. Xu, L. Peng, W. Gao, J. Ying, Z. Chen, C. Gao, *Carbon* **2018**, *133*, 316; c) J. Xi, Y. Li, E. Zhou, Y. Liu, W. Gao, Y. Guo, J. Ying, Z. Chen, G. Chen, C. Gao, *Carbon* **2018**, *135*, 44.

[8] a) Q. Wei, S. Pei, X. Qian, H. Liu, Z. Liu, W. Zhang, T. Zhou, Z. Zhang, X. Zhang, H. M. Cheng, W. Ren, *Adv. Mater.* **2020**, *32*, 1907411; b) Y. Liu, J. Zeng, D. Han, K. Wu, B. Yu, S. Chai, F. Chen, Q. Fu, *Carbon* **2018**, *133*, 435.

[9] a) A. Scidà, S. Haque, E. Treossi, A. Robinson, S. Smerzi, S. Ravesi, S. Borini, V. Palermo, *Mater. Today* **2018**, *21*, 223; b) P. N. Nirmalraj, T. Lutz, S. Kumar, G. S. Duesberg, J. J. Boland, *Nano Lett.* **2011**, *11*, 16.

[10] a) S. Böhm, *Nat. Nanotechnol.* **2014**, *9*, 741; b) K. Cao, S. Feng, Y. Han, L. Gao, T. H. Ly, Z. Xu, Y. Lu, *Nat. Commun.* **2020**, *11*, 284.

[11] L. Dong, Z. X. Chen, X. X. Zhao, J. J. Ma, S. Lin, M. X. Li, Y. Bao, L. Q. Chu, K. Leng, H. B. Lu, K. P. Loh, *Nat. Commun.* **2018**, *9*, 76.

[12] V. Georgakilas, M. Otyepka, A. B. Bourlinos, V. Chandra, N. Kim, K. C. Kemp, P. Hobza, R. Zboril, K. S. Kim, *Chem. Rev.* **2012**, *112*, 6156.

[13] J. N. Coleman, *Acc. Chem. Res.* **2013**, *46*, 14.

[14] M. Lotya, Y. Hernandez, P. J. King, R. J. Smith, V. Nicolosi, L. S. Karlsson, F. M. Blighe, S. De, Z. M. Wang, I. T. McGovern, G. S. Duesberg, J. N. Coleman, *J. Am. Chem. Soc.* **2009**, *131*, 3611.

[15] G. Bepete, E. Anglaret, L. Ortolani, V. Morandi, K. Huang, A. Pénicaud, C. Drummond, *Nat. Chem.* **2017**, *9*, 347.

[16] J. Hou, Y. Zheng, Y. Su, W. Zhang, T. Hoshide, F. Xia, J. Jie, Q. Li, Z. Zhao, R. Ma, T. Sasaki, F. Geng, *J. Am. Chem. Soc.* **2015**, *137*, 13200.

[17] a) G. Xin, T. Yao, H. Sun, S. M. Scott, D. Shao, G. Wang, J. Lian, *Science* **2015**, *349*, 1083; b) G. Xin, W. Zhu, Y. Deng, J. Cheng, L. T. Zhang, A. J. Chung, S. De, J. Lian, *Nat. Nanotechnol.* **2019**, *14*, 168.

[18] H. Y. Ma, H. Y. Geng, B. W. Yao, M. M. Wu, C. Li, M. Zhang, F. Y. Chi, L. Y. Qu, *ACS Nano* **2019**, *13*, 9161.

[19] a) Y. Xiao, Z. Xu, Y. Liu, L. Peng, J. Xi, B. Fang, F. Guo, P. Li, C. Gao, *ACS Nano* **2017**, *11*, 8092; b) T. Chen, Y. Xue, A. K. Roy, L. Dai, *ACS Nano* **2014**, *8*, 1039.

[20] Y. J. Wan, X. Y. Wang, X. M. Li, S. Y. Liao, Z. Q. Lin, Y. G. Hu, T. Zhao, X. L. Zeng, C. H. Li, S. H. Yu, P. L. Zhu, R. Sun, C. P. Wong, *ACS Nano* **2020**, *14*, 14314.

[21] F. Shahzad, M. Alhabeb, C. B. Hatter, B. Anasori, S. M. Hong, C. M. Koo, Y. Gogotsi, *Science* **2016**, *353*, 1137.

[22] J. Liu, H. Bin Zhang, R. Sun, Y. Liu, Z. Liu, A. Zhou, Z. Z. Yu, *Adv. Mater.* **2017**, *29*, 1702367.

[23] a) L. X. Liu, W. Chen, H. Bin Zhang, Q. W. Wang, F. Guan, Z. Z. Yu, *Adv. Funct. Mater.* **2019**, *29*, 1905197; b) F. Liu, Y. Li, S. Hao, Y. Cheng, Y. Zhan, C. Zhang, Y. Meng, Q. Xie, H. Xia, *Carbohydr. Polym.* **2020**, *243*, 116467.